Electronic Supplementary Information (ESI)

4-Fluorobenzyl Cyanide, Sterically-Hindered Solvent Expediting Interfacial Kinetics in Lithium-ion Batteries

Mingsheng Qin [a,b], Ziqi Zeng [a,*], Qiang Wu [a], Xiaowei Liu [c], Qijun Liu [a,b], Shijie Cheng [a] and Jia Xie [a,*]

a State Key Laboratory of Advanced Electromagnetic Technology, School of Electrical and Electronic Engineering, Huazhong University of Science and Technology, Wuhan 430074, Hubei (China)
b State Key Laboratory of Materials Processing and Die & Mould Technology, School of Materials Science and Engineering, Huazhong University of Science and Technology, Wuhan 430074, Hubei (China)
c State Key Laboratory of Advanced Technology for Materials Synthesis and Processing, Wuhan University of Technology, Wuhan 430074, Hubei (China)

Corresponding author.
E-mail: xiejia@hust.edu.cn (Jia Xie), ziqizeng@hust.edu.cn (Ziqi Zeng)

Experimental

Materials: Lithium bis(fluorosulfonyl)imide (LiFSI, battery grade), $LiPF_6$ (battery grade), Lithium borate difluoroxalate (LiDFOB, ≥99%), dimethyl Carbonate (DMC, battery grade) and ethylene carbonate (EC, battery grade), fluoroethylene carbonate (FEC, battery grade) were purchased from Duoduo Chemical Reagent Co., Ltd. 4-fluorobenzyl cyanide (FBCN, 99%) was purchased from Shanghai Macklin Biochemical Technology Co., Ltd. Carboxymethylcellulose (CMC) and PVDF binder were obtained from Aladdin. Lithium chips (14mm diameter, 0.5 mm thickness) and Separators (Celgard 2400) were purchased from China Energy Lithium Corp. The electrolyte was prepared in glove box (O_2 and H_2O contents < 0.1 ppm) based on molar ratio. For example, LiFSI-9FBCN was prepared by dissolving 1 molar LiFSI in 9 molar FBCN. The CCE electrolyte was prepared by dissolving 1 M $LiPF_6$ in mixed EC and DMC (1:1 vol%) solvents. The FBCN-based electrolyte and EC-based electrolyte were formulated by adding 2wt% FEC and 2wt% LiDFOB into LiFSI-9FBCN and CCE. FBCN+FEC and FBCN+LiDFOB were prepared by adding 2wt% FEC and 2wt% LiDFOB separately into LiFSI-9FBCN. For electrode preparation, the slurry was prepared by mixing graphite, Super P, and CMC at mass ratio of 8: 1: 1. The slurry was casted on Cu foil and dried at 80 °C. The mass loading is 2~3 mg cm^{-2}. The cathode was prepared by mixing $LiFePO_4$, Super P and PVDF at mass ratio of 8: 1: 1. The slurry was casted on carbon-coated Al and dried at 80 °C with mass loading of 2.5~4 mg cm^{-2}. The $LiFePO_4$//graphite pouch cell was assembled in practical conditions ($LiFePO_4$ area capacity: 3.2 mAh cm^{-2}, electrolyte: 3 g Ah^{-1}, N:P=1.1:1) for long-term cycling at 0.33C. This pouch cell was purchased from Canrd Technology Co. Ltd and the detailed information for electrode fabrication are business secret. The nominal capacity is designed as 1.6 Ah. Home-made $LiFePO_4$//graphite pouch cells ($LiFePO_4$ mass loading: 4 mg cm^{-2}) were used for accessing rate capability only.

Materials characterizations: XRD patterns were collected by X-ray Powder diffractometer (Rigaku MiniFlex600). The recorded 2Theta ranges from 10^{o} to 70^{o} at a scan rate of 5^{o} min^{-1}. The SEM images were obtained on Nova NanoSEM 450. The graphite for SEM was disassembled from cycled graphite//Li cells at a rate of 0.2C after 50 cycles. The XPS was carried out on an AXIS-ULTRADLD-600W. NMR results were carried out with Ascend 600 MHZ (Bruker. Co., Ltd.). The targeted electrolytes (500 μL) were transferred into the NMR tube in glovebox (O2 and H2O contents < 0.1 ppm). The 100 μL NMR solvent (deuterated water) was hot sealed in a capillary tube, which was then coaxially immersed into the NMR tube for locking field. Note that the NMR solvent was not mixed directly with electrolyte for avoiding interactions. The ^{1}H-NMR spectra were acquired using typical standard parameters of one pulse sequence with a recycle delay of 2 s, and 16 number of scans. The signal of deuterated water was used for calibration in ^{1}H-NMR results. The thermal properties of electrolyte were studied by DSC4000 (PerkinElmer, America) at a rate a 10 ^{o}C min^{-1}, with an initial scan to low temperature and a reversed scan to high temperature.

Electrochemical measurements: CR2032 coin cells were assembled for graphite//Li and $LiFePO_4$//Li cells in an Argon-filled glovebox with H_2O and O_2 contents below 0.1 ppm. Different electrolytes were employed for assessing the electrochemical performance. All coin cells (CR2032) were tested on Neware Battery Measurement System at ambient temperature unless otherwise stated. Cyclic voltammetry (CV) curves were tested by CHI 600D at a scan rate of 0.1 mV s^{-1}. Linear sweep voltammetry (LSV) was performed by CHI 600D. The Electrochemical impedance spectroscopy (EIS) measurements were measured by a Bio-Logic SP-300. The $LiFePO_4$//graphite pouch cell was tested by charging at 0.33C and discharging at 0.33C at ambient environment. The activation energy for desolvation was calculated based on the EIS measurements in a wide temperature range. Before impedance test, the cells were precycled for 5 cycles between 0.01 and 2 V to ensure a completion of SEI formation. Then the cells were held at 0.15 V until the residual current drops below 0.01 C. Next, EIS measurements were performed in the frequency range from 10^5 to 10^{-1} Hz with a voltage amplitude of 10 mV for graphite//graphite cell. The energies corresponding to Li^+ transport across SEI and charge transport were derived from R_{sei} and R_{ct}, respectively, with assumption that each step involves a thermally activated process.

$$\frac{1}{R_{(ct,\ sei)}} = A_0 e^{-E_a/RT}$$

Where A_0, R and E_0 represent pre-exponential constant, standard gas constant and the activation energy, respectively. The slopes of $log(R_{ct}^{-1})$ vs reciprocal temperature $1/T$ plots one can lead to activation energies as

$$E_a = -19.144 \times slop(kJ\ mol^{-1})$$

Theoretical calculations: The density functional theory (DFT) calculations for stripping species from Li^+ solvation were carried out in the DMol3 package of Materials Studio 2018. DFT calculations of molecular systems for isolating Li^+ from varied solvates were conducted using the Gaussian 16 package. The geometry optimization was performed at the B3LYP/6-311+G(d,p) level, incorporating Grimme's D3 dispersion energy correction. Additionally, all calculated energies were adjusted using a zero energy correction. The energy for isolating Li^+ (ΔE) was obtained by $\Delta E = E_{Li+-solvents} - E_{solvents} - E_{Li+}$. The calculations of adsorption energy on graphite (001) plane were carried out in the CASTEP package. In DMol3 package, the exchange-correlation potential was treated by using a mixed-generalized gradient approximation (m-GGA) with the Perdew-Burke-Ernzerhof (PBE) parametrization. A cutoff energy of 450 eV was set. The electronic energy was considered self-consistent when the energy change was smaller than 10−5 eV, while the tolerance convergence in ionic was 10-5 eV, too. Furthermore, the van der Waals correction of Grimme's DFT-D3 model was adopted. In CASTEP package, the cell lattice of size 17.22 Å X 17.22 Å X 15 Å was built, with a K-point value of 1 X 1 X 1.

The required energy (E_{ds}) for stripping individual species from Li^+ solvates was defined as:

$$E_{ds} = E_{solvent} + E_{Li^+} - E_{complex}$$

Where $E_{complex}$ is the energy of the LiFSI-solvent (referred as FBCN and EC) complex, $E_{solvent}$ is the energy of the solvent molecule and E_{Li^+} is the energy of bare Li^+ ion. The detailed calculations are listed in the corresponding paragraph.

The adsorption energy of different solvent molecules on graphene (E_{ad}) was defined as:

$$E_{ad} = E_{(adsorption\ system)} - E_{graphene} - E_{solvent}$$

Where $E_{(adsorption\ system)}$ is the energy of system that solvent molecules are adsorbed on graphene, $E_{graphene}$ is the energy of the established graphene surface plane, $E_{solvent}$ is the energy of the solvent molecule.

As for the adsorption of solvents on the edge plane of graphite (Graphite (010)), the first-principles DFT calculations were performed using the projector-augmented wave (PAW) method and the Perdew-Burke-Ernzerhof (PBE) exchange-correlation functional as implemented in the Vienna Ab-initio Simulation Package (VASP). To describe the effects of the long-range van der Waals interactions, a semiclassical dispersion correction scheme (DFT-D3) was used. The plane-wave energy cutoff was set to 450 eV, and the convergence threshold for the iteration in a self-consistent field was set at 10-6 eV. All of the atoms were allowed to fully relax until the forces exerted on each atom were less than 0.01 eV/Å during structural optimization. The calculated equilibrium lattice constants for graphite was 2.465 Å, 2.465 Å, and 6.58403 Å. The model of the edge plane of graphite (Graphite (010)) contain 4 layers of a 3 × 5 supercell, and the dangling bonds on the surface are saturated and terminated with hydrogen atoms. To avoid artificial interaction between layers, a vacuum spacing of ~20 Å was applied. The top 2 layers carbon atoms were relaxed at the bulk crystal geometry during structural optimization. A Gaussian smearing of 0.1 eV was applied for optimizations and a k-point grid with 2 × 3 × 1 Gamma centered mesh for sampling the first Brillouin zone.

The molecular electrostatic potential (ESP): The molecular geometries for the ground states were optimized by DFT at the GGA Functional with BLYP, and then the energy, orbital levels and ESPs of molecules were evaluated at the GGA Functional with BLYP as well. All the DFT calculations were carried out with the DMol3 package of Materials Studio (2018 version). The physical meaning of the electrostatic potential itself: the amount of work required to pull an entire charge from infinity to a position on the graph, with positive values representing positive work and negative values representing negative work. ESP_{max} and ESP_{min} represent the maximum and minimum values of work done, respectively, denoting the most positive and negative part on molecular respectively. It is of great significance for investigating electrostatic interactions between molecules, predicting reaction sites and predicting molecular properties.

MD simulations were conducted with a Materials Studio software, reversion 2018 with COMPASS II force field. The MD simulation package Forcite was used. The Ewald summation method was used for the electrostatic interactions between the permanent charges with either permanent charges or induced dipole moments with k=63 vectors. And multiple time step integration was employed with an inner time step of 0.5 fs (bonded interactions), a central time step of 1.5 fs for all non-bonded interactions within a truncation distance of 8.0 Å and an outer time step of 3.0 fs for all non-bonded interactions between 7.0 Å and the non-bonded truncation distance of 14 – 16 Å. The reciprocal part of Ewald was calculated every 3.0 fs. A Nose–Hoover thermostat was used to control the temperature with the associated frequencies of 10–2 and 0.1×10–4 fs. a Berendsen barostat was used to control the pressure with a decay constant of 0.1 ps. The atomic coordinates were saved every 2 ps for post-analysis. Initial equilibration runs of ~5 ns were performed in an isobaric isothermal simulation (NPT) ensemble to obtain the equilibrium box size that is used in the follow-up equilibration and production runs of ~1 ns performed in the isochoric isothermal simulation (NVT) ensemble.

Other statements: Note that DFT relies heavily on reasoning by analogy, simplified model and conceptualization. The practical condition is more complicated since the defects and contaminations on graphite surface, electric field and SEI construction. These interruptions are all discarded in DFT simulation. We used a simplified, idealized and conceptual model for easy calculation in electrolyte research, which helps with better understanding interfacial behaviors and solvent's properties. Moreover, the calculated energy in Figure 5a and 5b doesn't represent the exact desolvation energy, but helps with understanding the stability of varied solvates. These values differ based on varied calculation model and process, but the always lower energy for FBCN-involved solvates indicate its good kinetics compared to EC-involved solvates.

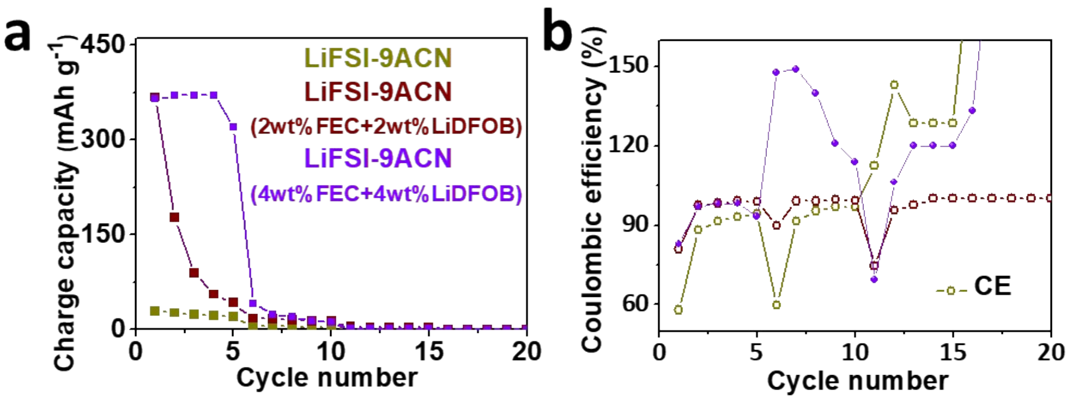

Figure S1. (a) Reversible capacities and (b) Coulombic efficiencies of Li//graphite cells in ACN-based electrolytes. The introduction of additives into LiFSI-9ACN (LiFSI: ACN, molar ratio of 1: 9) exerts limited effects for interfacial compatibility, highlighting the importance of electrolyte structure (e.g., Li$^+$-ACN binding strength and coordination number).

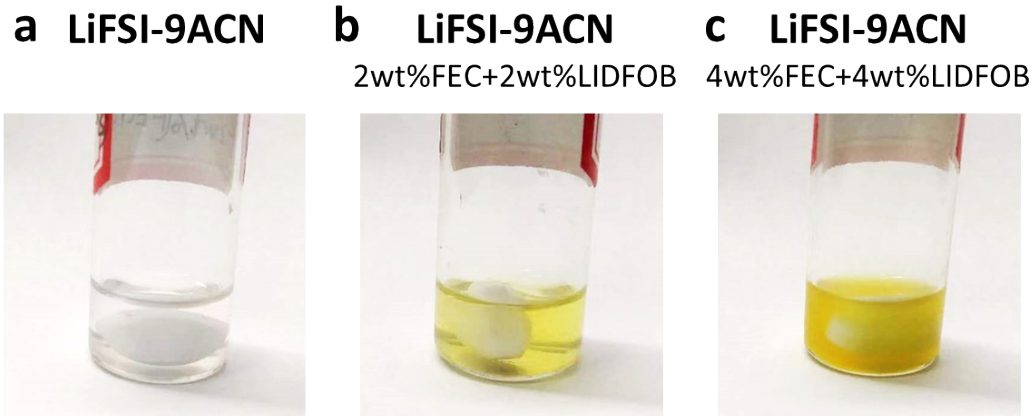

Figure S2. Pictures for various ACN-based electrolytes after 10 days at ambient temperature. Additives lead to electrolyte degradation as denoted by the color change. These results indicate that ACN cannot be used as main solvent in electrolyte. In contrast, the FBCN-based electrolyte exhibits good stability and electrochemical performance, highlighting the significance of steric hindrance.

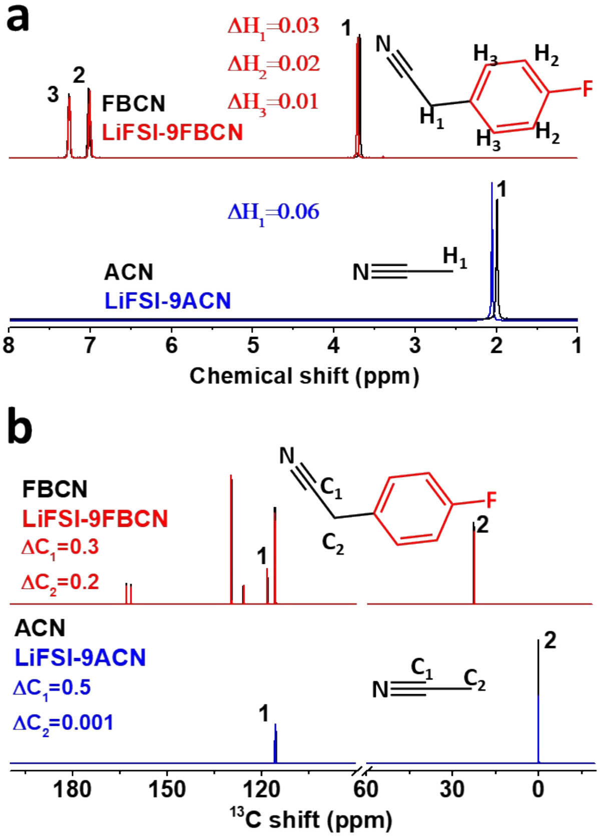

Figure S3. (a) ^{1}H shifts and (b) ^{13}C shifts for various solutions. The deviations for different atoms after Li salts' dissociation are listed. The lower ΔH_1 and ΔC_1 values for FBCN indicates weaker interaction with Li^+ compared to ACN (fixing molar ratio for LiFSI: solvents as 1:9).

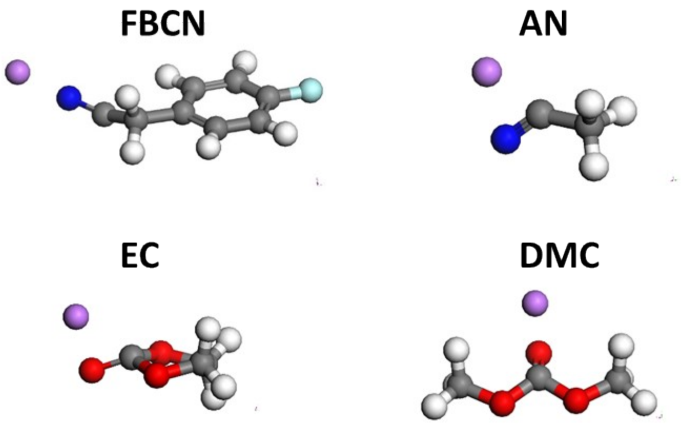

Figure S4. The optimized configurations during calculating binding energies for FBCN, ACN, ethylene carbonate (EC) and dimethyl carbonate (DMC) with Li^+.

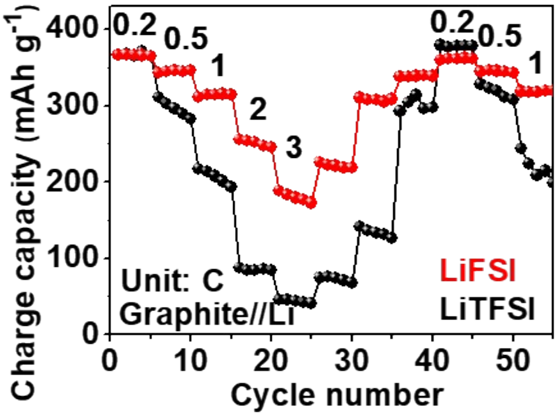

Figure S5. The rate performance of graphite//Li cells in FBCN-based electrolytes with varied Li salts. A similar capacity is obtained at low current density (0.2 C). However, the inferior capacity is delivered in LiTFSI-based electrolyte at high rates since its lower conductivity compered to LiFSI-based electrolyte.

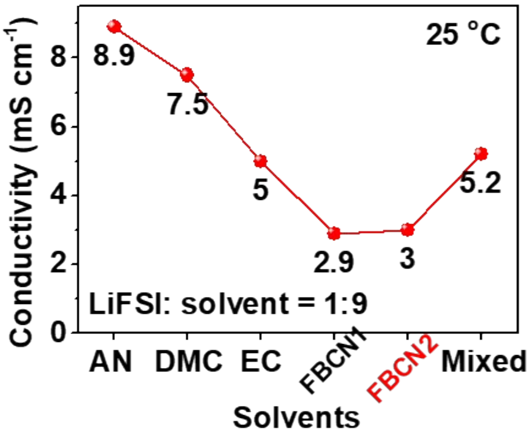

Figure S6. Conductivities for LiFSI in varied solvents (fixing LiFSI: solvent molar ratio at 1:9, FBCN1 denotes pure FBCN, FBCN2 denotes FBCN-based electrolyte (2 wt% FEC and 2 wt% LiDFOB), Mixed denotes DMC: FBCN molar ratio of 4.5:4.5). First, FBCN1 shows lower conductivity than other solvents, indicating its weak solvating ability and poor Li salts' dissociation capability. Second, the additives in FBCN2 exert negligible effects for improving its conductivity since their limited contents. Third, the combination of FBCN with linear carbonates (e.g., DMC) will improve ionic conductivity, which inspires that formulating eutectic solution might ameliorate unsatisfied conductivity in FBCN solvent.

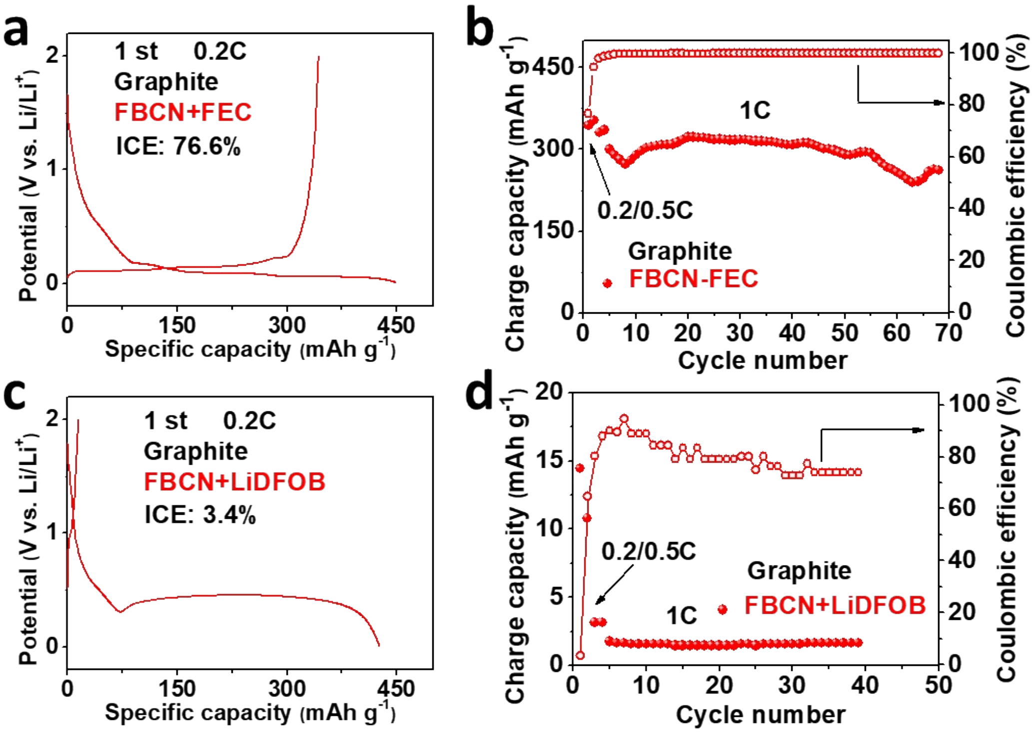

Figure S7. (a, c) Initial charge-discharge curves and (b, d) cycling stabilities for graphite//Li cells in single FEC (LiFSI-9FBCN with 2wt% FEC) and LiDFOB-modified (LiFSI-9FBCN with 2wt% LiDFOB) electrolytes. A fluctuating cycling with inferior ICE (76.6%) and capacity (318 mAh g^{-1}, 1C) is observed for FBCN+FEC compared to FBCN-based electrolyte (86.7%, 348 mAh g^{-1}, 1C), indicating the unstable interfacial passivation and possible electrolyte decomposition during cycling. Graphite in FBCN+LiDFOB shows endless discharging and no reversible capacity, indicating incompetent SEI derived from LiDFOB.

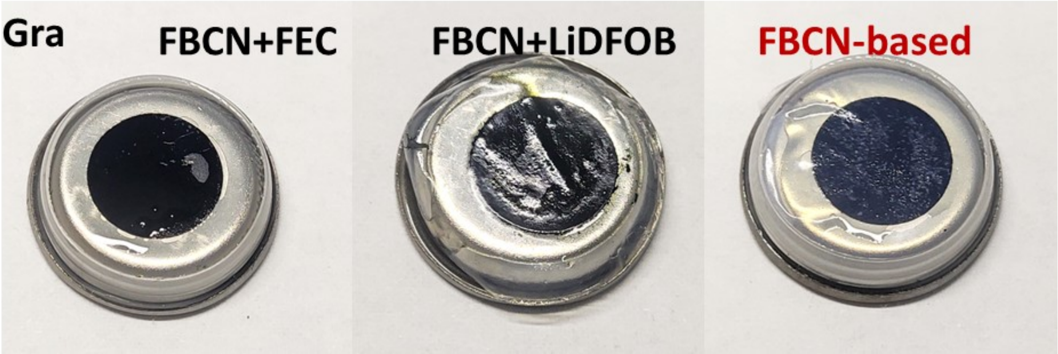

Figure S8. Pictures for cycled graphite in different electrolytes. A flat and smooth surface is observed for FBCN+FEC and FBCN-based electrolytes while a rough and sticky surface is formed in FBCN+LiDFOB, indicating the interfacial incompatibility and accumulation of byproducts even after LiDFOB modification.

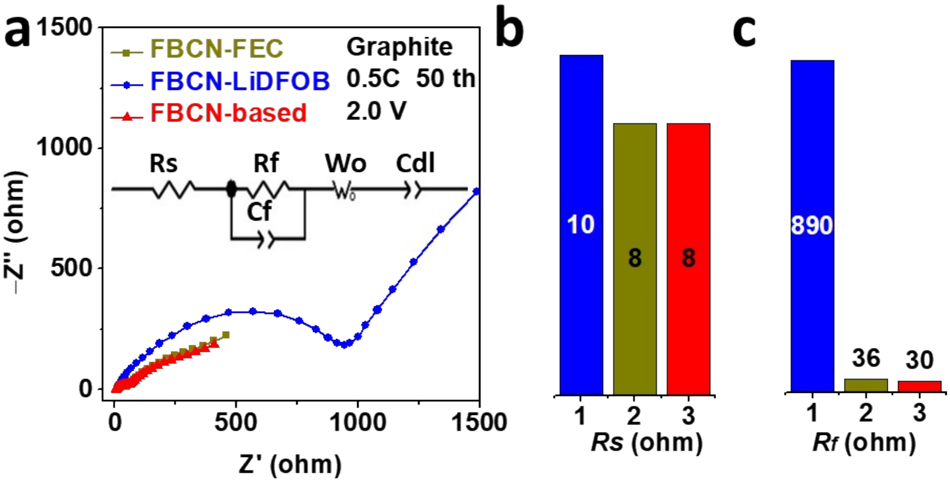

Figure S9. (a) EIS results and (b) exact impedance for each part for cycled graphite in varied electrolytes. The highest interfacial resistance is noticed in FBCN+LiDFOB electrolyte, which is consistent with previous results, indicating sluggish interfacial kinetics.

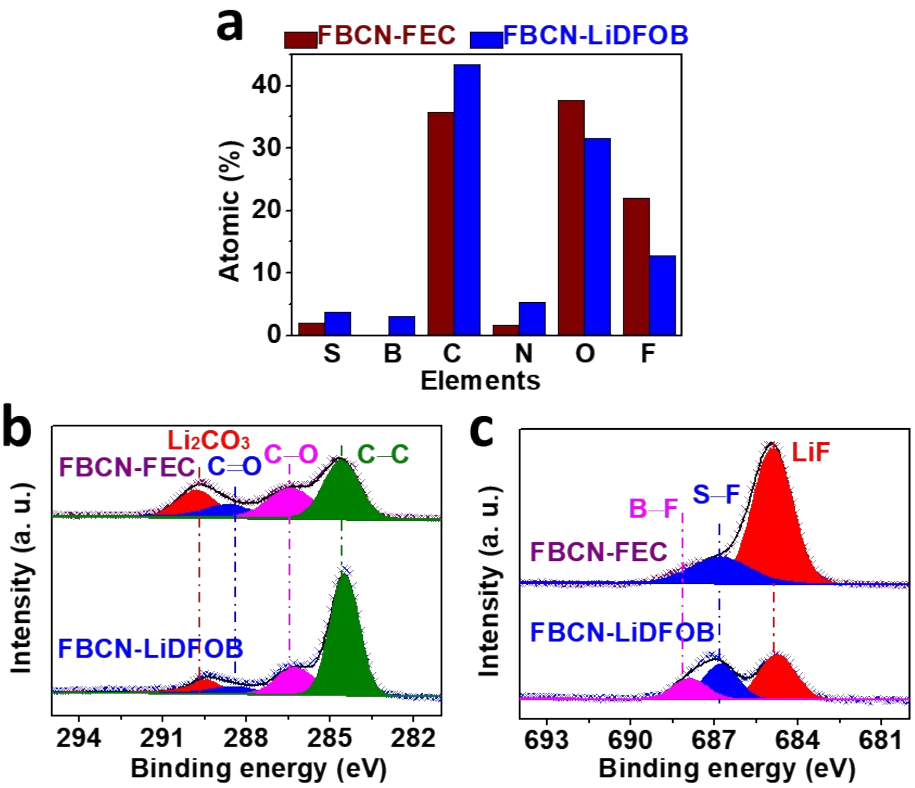

Figure S10. (a) Elemental distribution and XPS results for (b) C 1s and (c) F 1s on graphite. A higher content of S and N indicates severe Li salts decomposition in FBCN+LiDFOB. The signal of B in FBCN+LiDFOB denotes LiDFOB-modified interfacial chemistry, which nevertheless cannot enable reversible cycling. The higher F content in FBCN+FEC is caused by the preferential decomposition of FEC, leading to LiF-rich SEI with less decomposition of anions (S-F). Moreover, the C=O, C-O and Li_2CO_3 species are substantially inhibited in FBCN+LiDFOB, indicating that LiDFOB is helpful for inhibiting solvent's decomposition despite it's useless for reversible cycling.

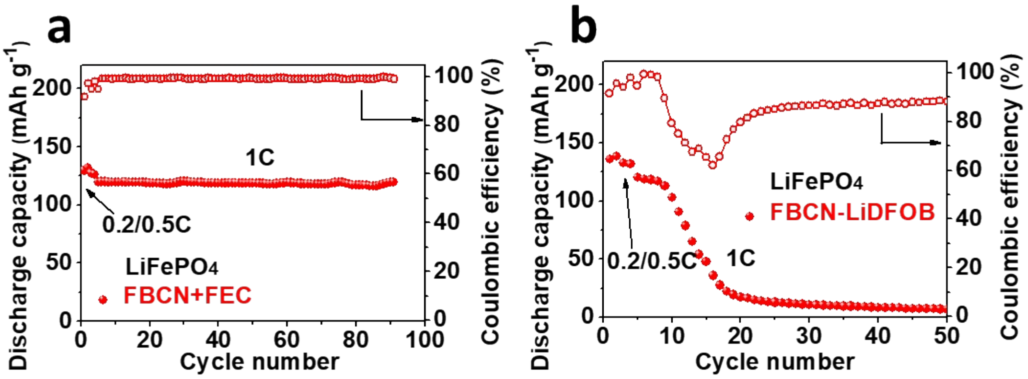

Figure S11. Cycling stabilities for LiFePO$_4$/Li cells in (a) FBCN+FEC and (b) FBCN+LiDFOB electrolytes. A fast capacity fading is presented for cell in FBCN+LiDFOB and a lower capacity is obtained for cell in FBCN+FEC (118 mAh g^{-1}, 1C) compared to FBCN-based electrolyte (140 mAh g^{-1}, 1C).

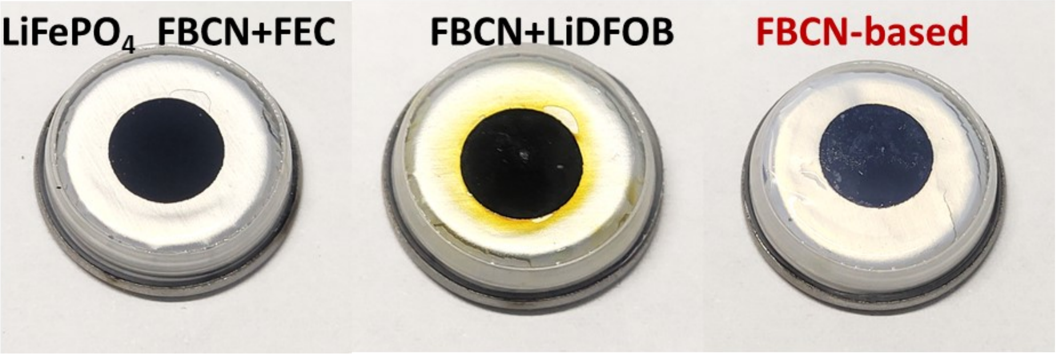

Figure S12. Pictures for cycled LiFePO$_4$ in varied electrolytes. The separator turns to be yellow in FBCN+LiDFOB, indicating severe electrolyte degradation.

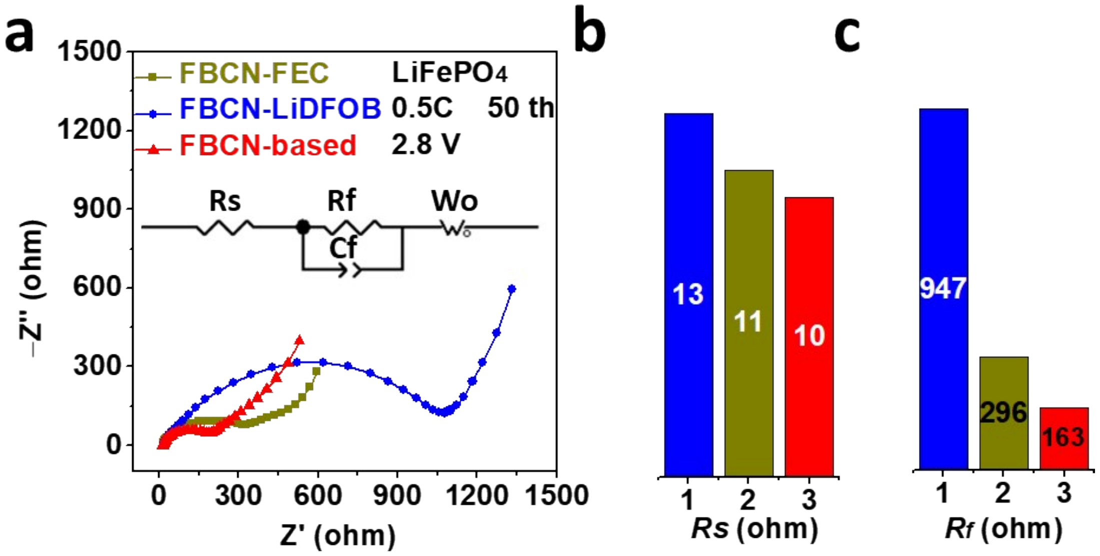

Figure S13. (a) EIS results and (b) impedance for $LiFePO_4$//Li cells in varied electrolytes. Only the combination of FEC and LiDFOB enables the lowest resistance.

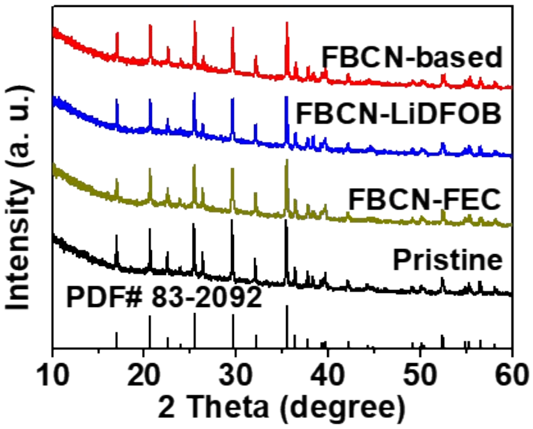

Figure S14. XRD patterns for $LiFePO_4$ cycled in varied electrolytes. Negligible structural derivations are noticed in all electrolytes, indicating the cell failure is mainly caused by interfacial degradations rather structural destruction.

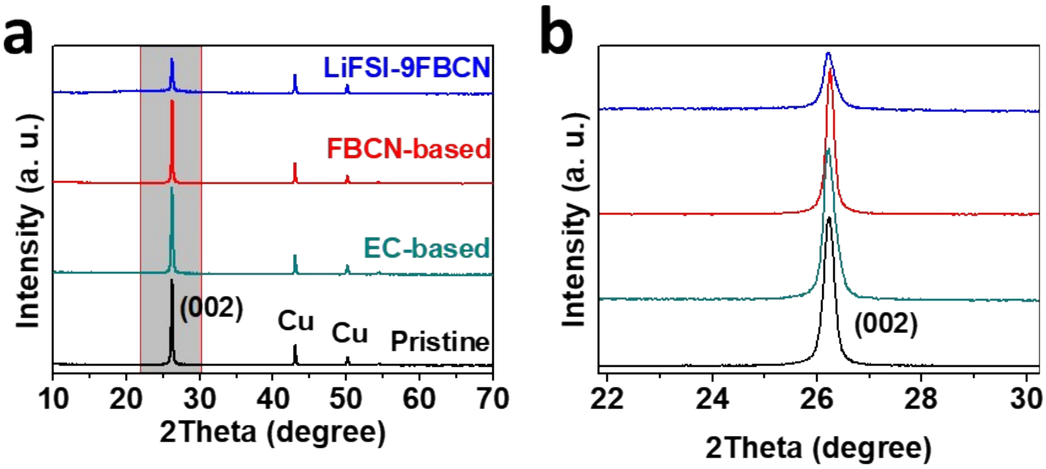

Figure S15. XRD patterns of graphite cycled in different electrolytes. (a) Full XRD pattern and (b) enlarged area. The (002) plane is substantially weakened after cycling in LiFSI-9FBCN, indicating destructed graphite lattice.

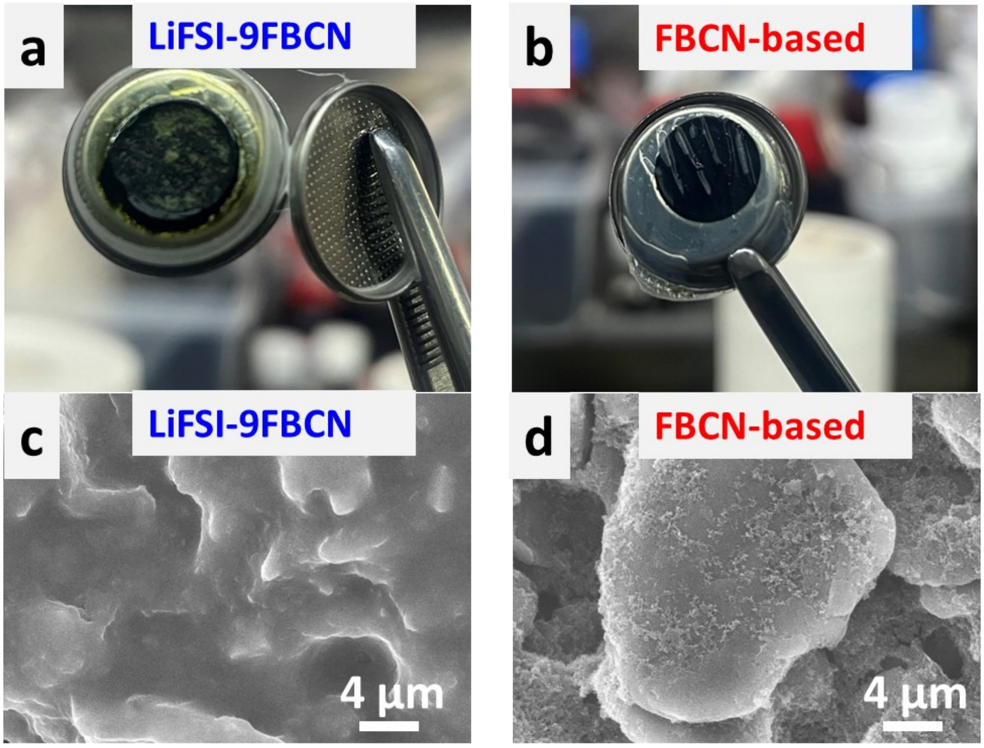

Figure S16. (a) Picture and (c) SEM image of graphite electrode cycled in LiFSI-9FBCN. (b) Picture and (d) SEM image of graphite cycled in FBCN-based electrolyte. The introduction of additives effectively prevents interfacial exacerbation in FBCN-based electrolyte.

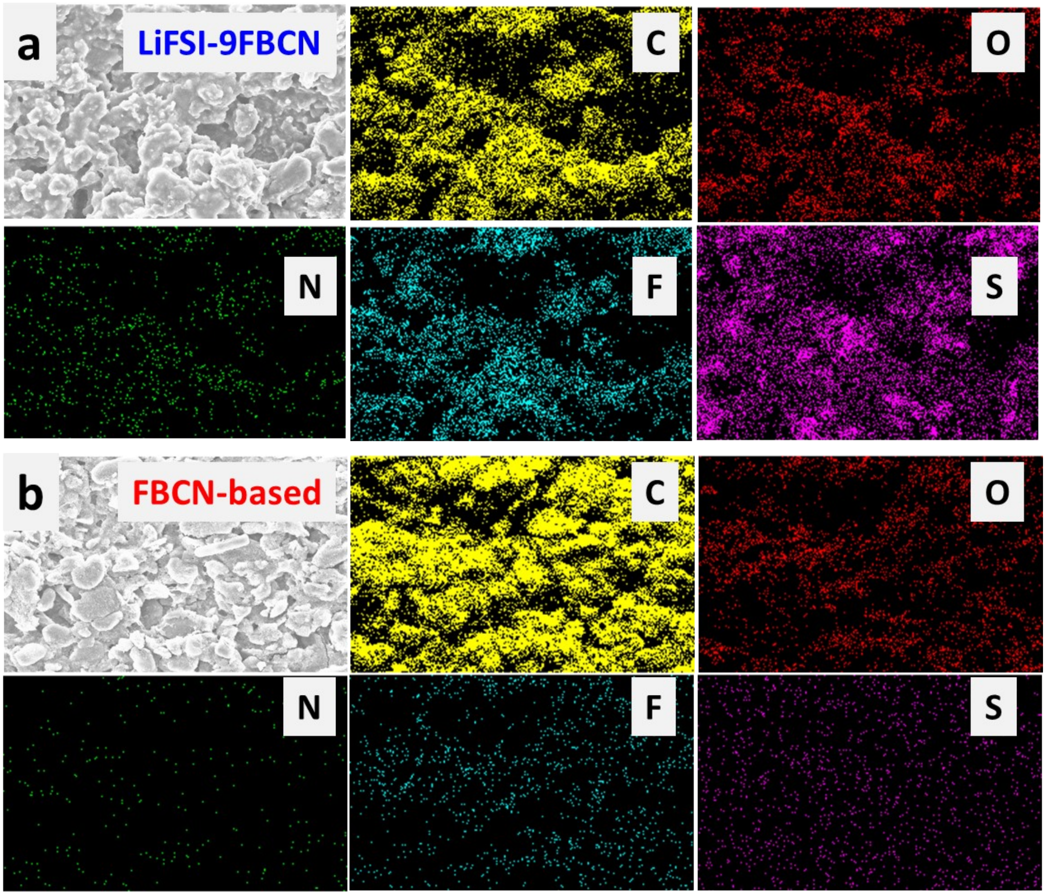

Figure S17. Elemental distributions for graphite cycled in (a) LiFSI-9FBCN and (b) FBCN-based electrolyte. Intensified elemental signals are detected for graphite in LiFSI-9FBCN, indicating severe electrolyte decomposition.

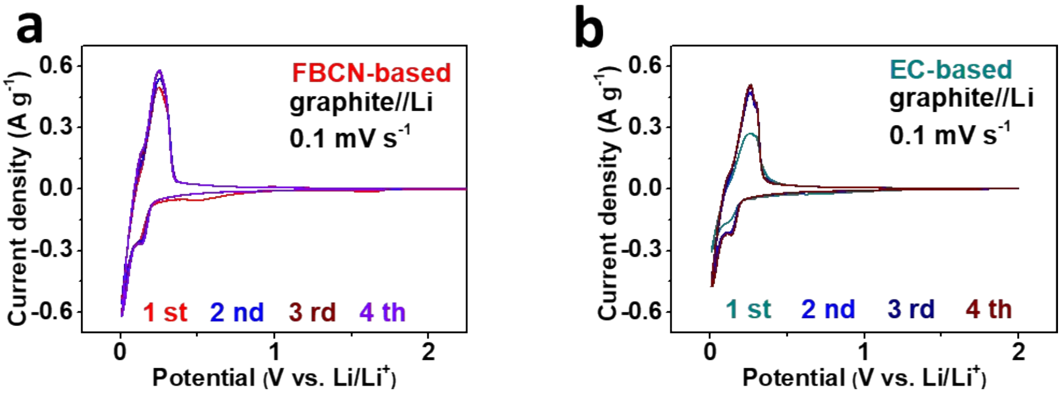

Figure S18. CV curves of graphite//Li cells in (a) FBCN-based electrolyte and (b) EC-based electrolyte.

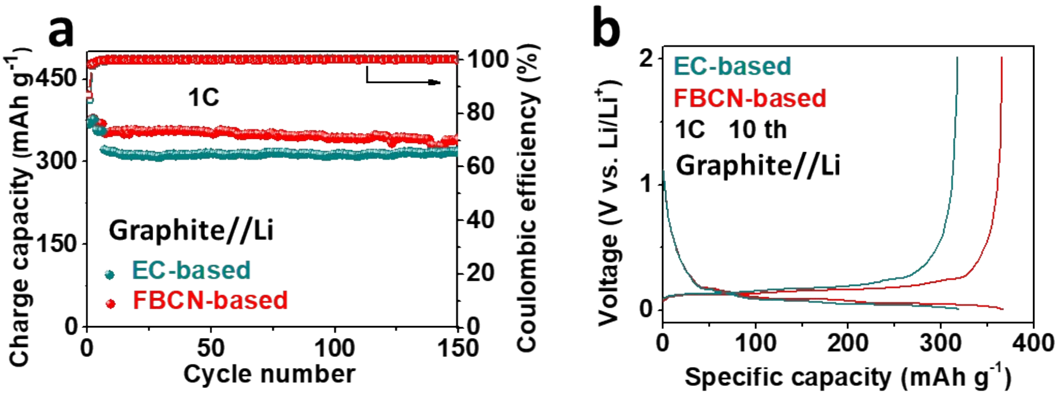

Figure S19. (a) Cycling stabilities and (b) charge-discharge curves of graphite//Li cells in different electrolytes. A higher capacity and lower polarization are obtained for cells in FBCN-based electrolyte

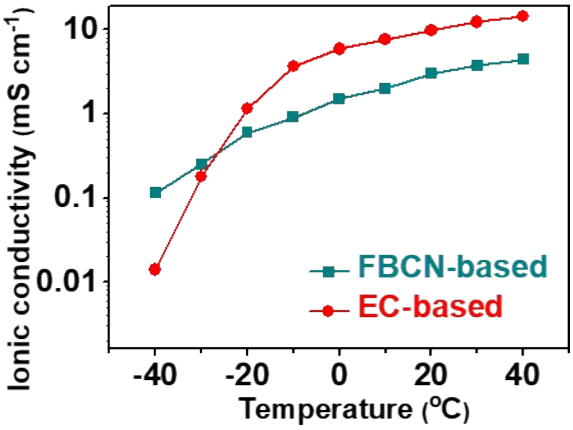

Figure S20. Conductivities for different electrolytes.

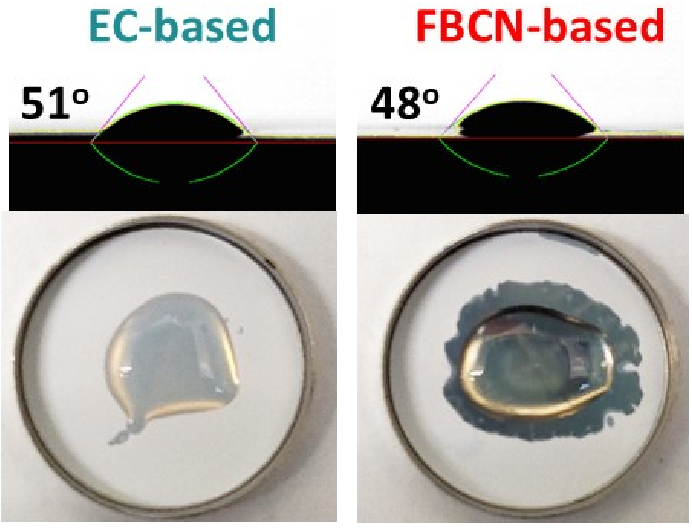

Figure S21. Wettability on PP separators

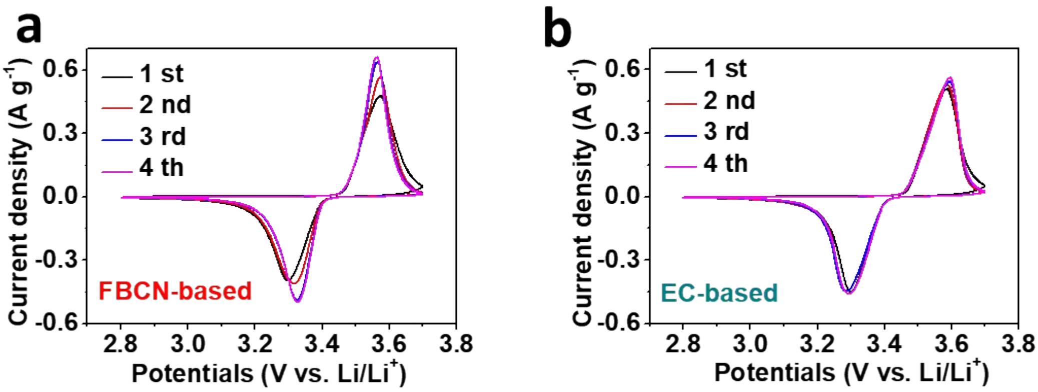

Figure S22. CV curves of $LiFePO_4$//Li cells in (a) FBCN-based and (b) EC-based electrolyte.

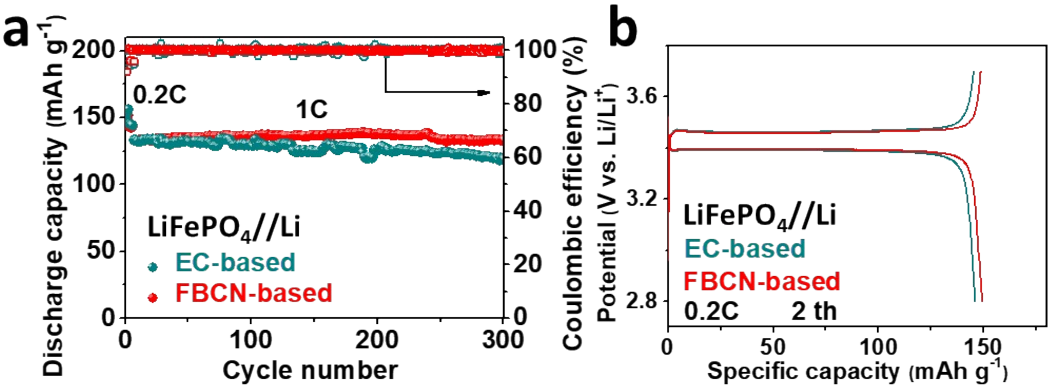

Figure S23. (a) Cycling stabilities and (b) charge-discharge curves of $LiFePO_4$//Li in different electrolytes.

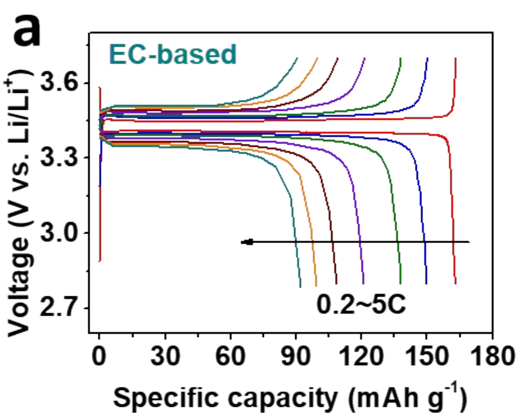

Figure S24. Charge-discharge curves for $LiFePO_4$//Li cells at varied rates in (a) EC-based and (b) FBCN-based electrolytes.

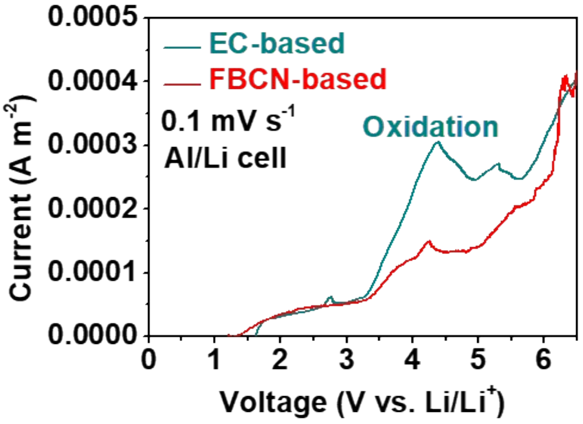

Figure 25. LSV results on Al//Li cells.

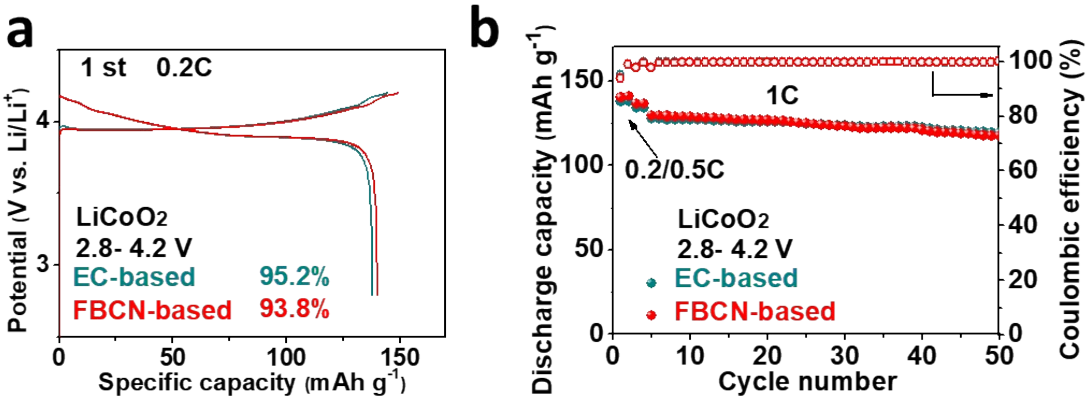

Figure 26. (a) Initial charge-discharge curves and (b) cycling performance for $LiCoO_2$ in varied electrolytes. A comparable cycling stability is obtained for both electrolytes, indicating negligible electrochemical degradation at cut-off voltage of 4.2 V.

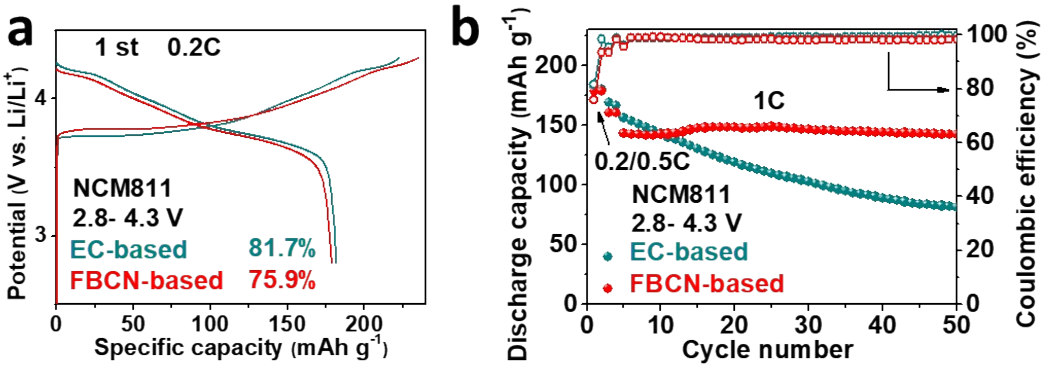

Figure 27. (a) Initial charge-discharge curves and (b) cycling performance for NCM811 in varied electrolytes. A fast capacity fading is noticed for NCM811 in EC-based electrolyte at 4.3 V, which is caused by its poor compatibility towards high-nickel cathode and inferior oxidative tolerance.

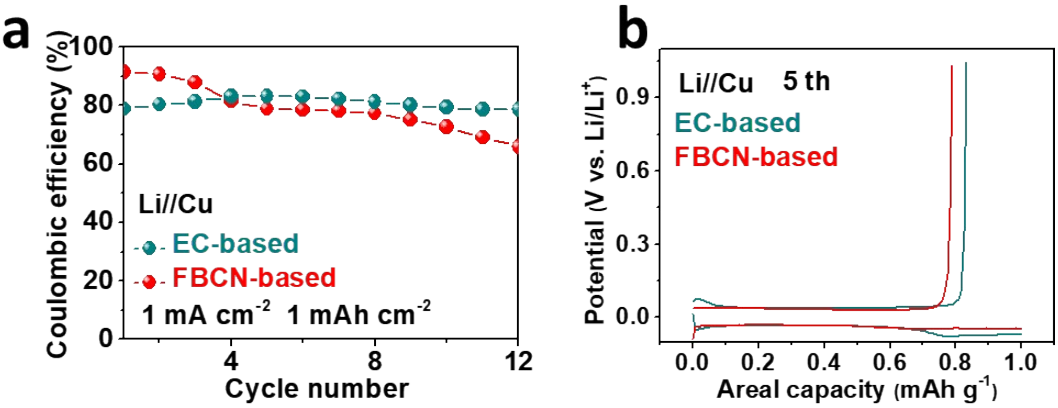

Figure S28. (a) CEs for Li//Cu cells and (b) corresponding curves in various electrolytes.

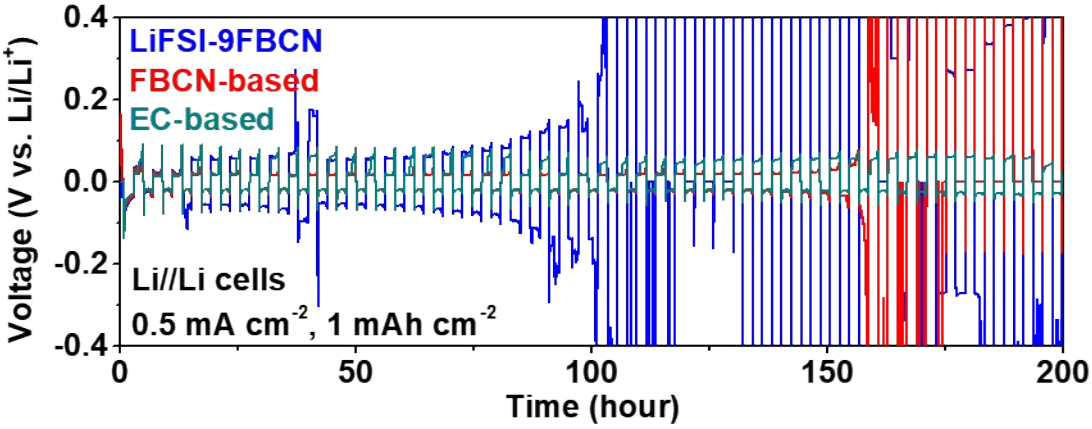

Figure S29. Performance for Li/Li symmetric cells in varied electrolytes. The cells in FBCN-based electrolytes cycles longer than that of LiFSI-9FBCN (without additives), indicating the interfacial passivation of additives. Moreover, the cell in FBCN-based electrolyte exhibits lower polarization than that of EC-based electrolyte at initial stage, indicating its facilitated dynamics. However, the cell failure happens after 160 hours in FBCN-based electrolyte, which originates from interfacial degradation.

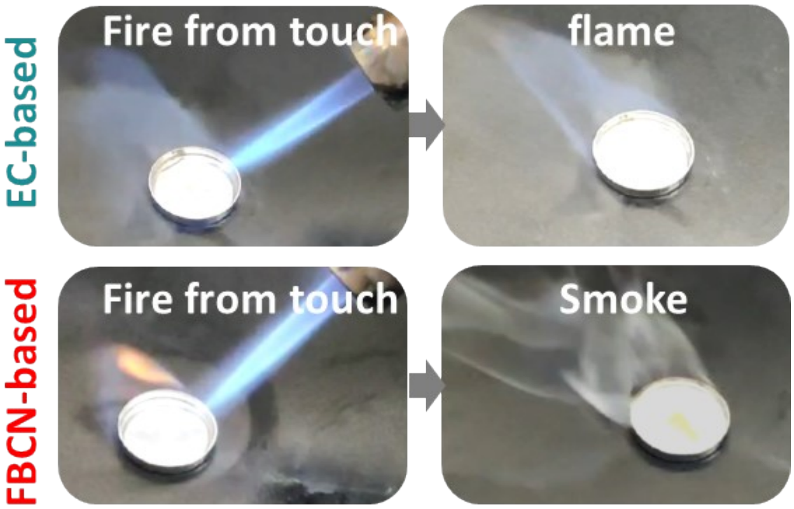

Figure S30. Flammability tests for different electrolytes (Ignited for 5 s and then removed fire).

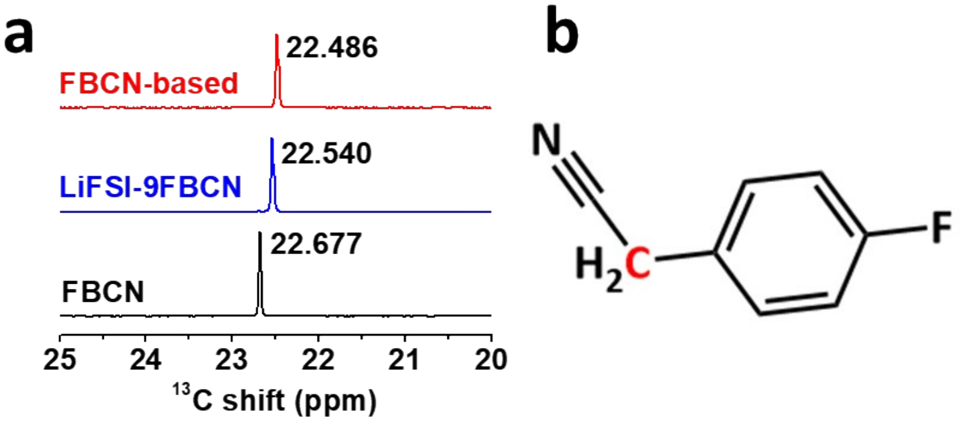

Figure S31. (a) ^{13}C-NMR results and (b) designated C in FBCN structure.

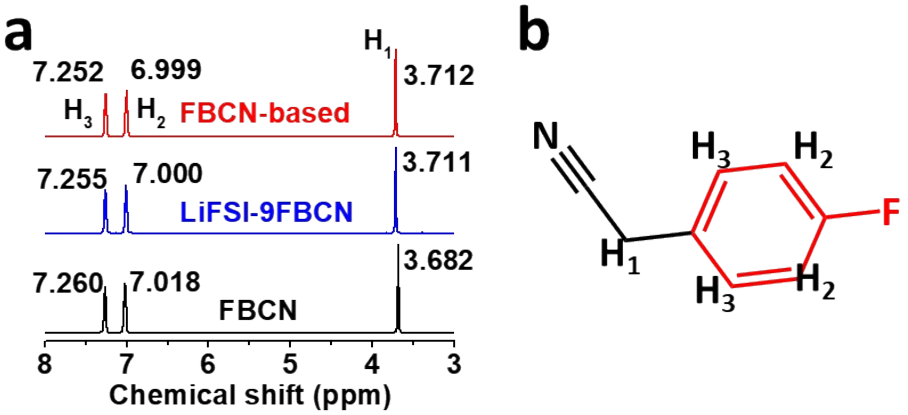

Figure S32. (a) ^{1}H-NMR results and (b) designated H in FBCN structure.

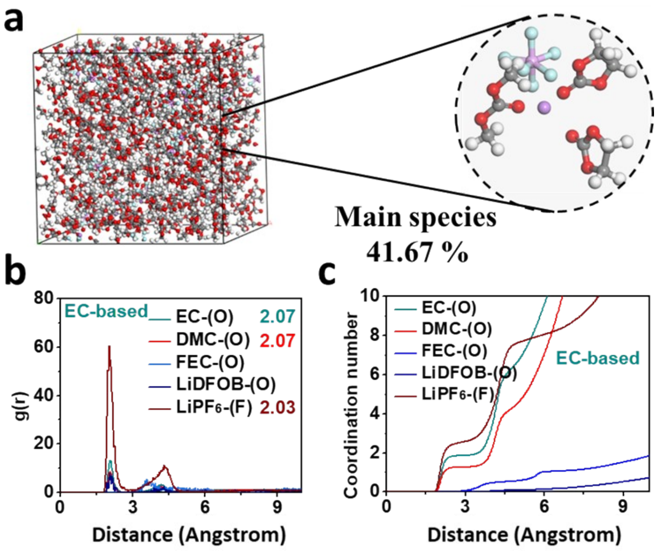

Figure S33. (a) Snapshot of AIMD simulation and main species in electrolyte. (b) Radial distributions and (c) coordination numbers for EC-based electrolyte.

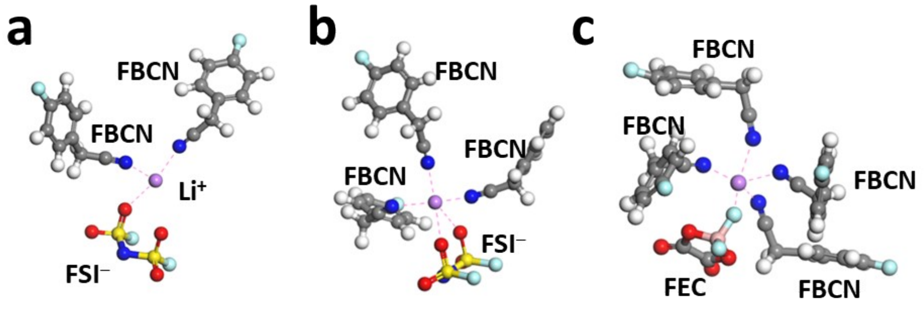

16.66 % **54.17 %** **29.17 %**

Figure S34. Individual species picked from AIMD simulations including (a) Li^+-2[FBCN]-[FSI^-], (b) Li^+-3[FBCN]-[FSI^-] and (c) Li^+-4[FBCN]-[FEC].

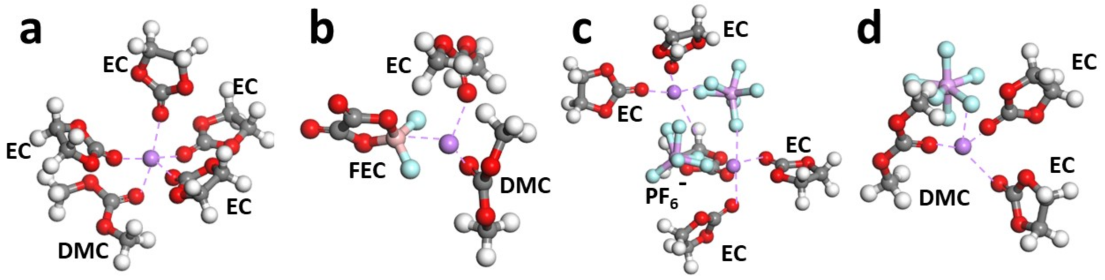

8.33 % **16.67 %** **33.33 %** **41.67 %**

Figure S35. Individual species picked from AIMD simulations for EC-based electrolyte. More species participate into Li^+ solvation for EC-based electrolyte while less ingredients are involved for FBCN-based electrolyte. The bulky FBCN cannot coordinate with Li^+ as closely as small-size EC and DMC, leading to less coordinated species in space-confined solvation shell as denoted by smaller average coordination number in FBCN-based electrolyte.

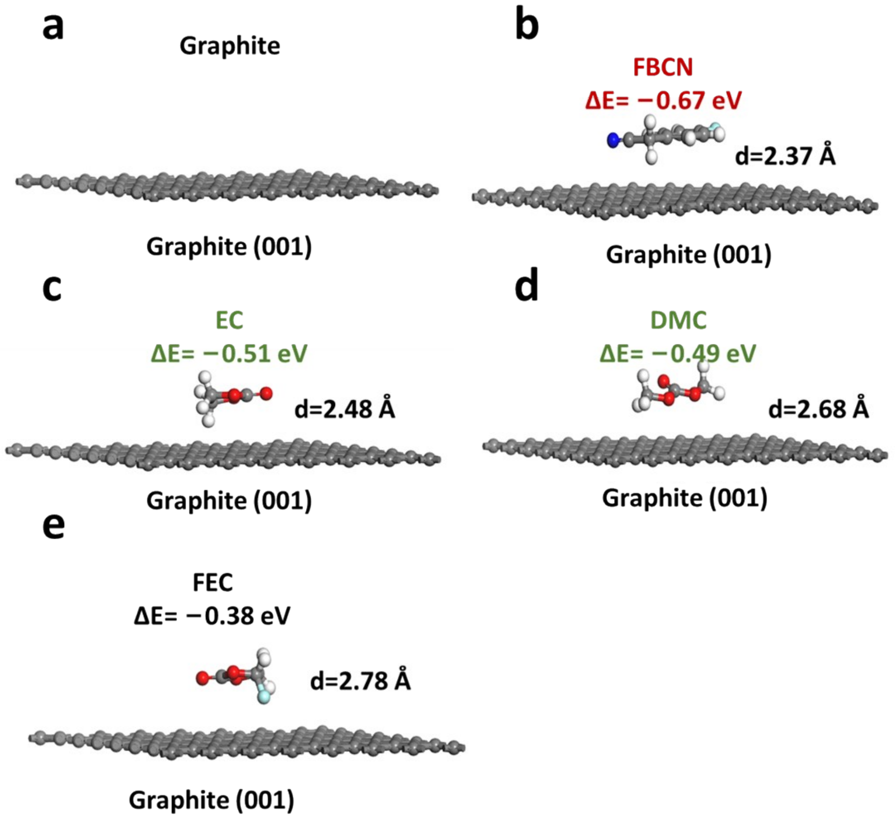

Figure S36. The optimized geometries for (a) graphite (001) plane, (b) FBCN, (c) EC, (d) DMC and (e) FEC on graphite (001) plane. The FBCN shows the lowest distance towards graphite, indicating its electrostatic superiority (π–π stacking mode). Furthermore, the calculated adsorption energy for FBCN, EC, DMC and FEC are −0.67, −0.51, −0.49, and −0.38 eV respectively, denoting the energetic favorability of FBCN on graphite (001) surface. These results indicate preferential of FBCN on graphite surface. The detailed calculations are listed in Table S2.

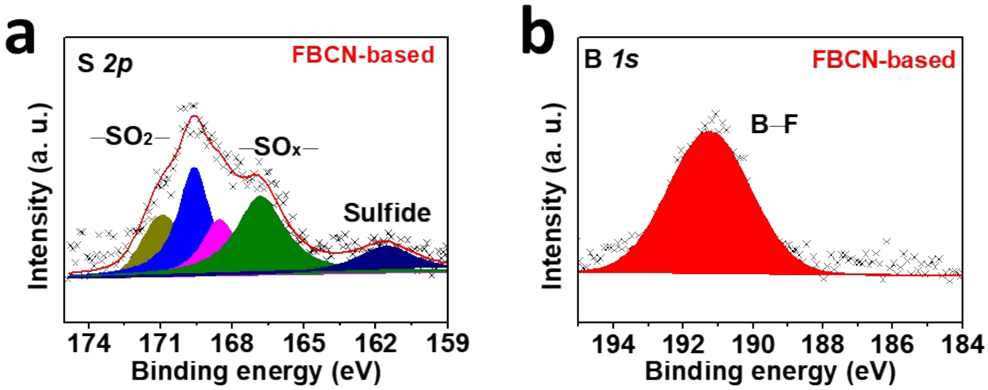

Figure S37. (a) S and (b) B signals for graphite cycled in FBCN-based electrolyte.

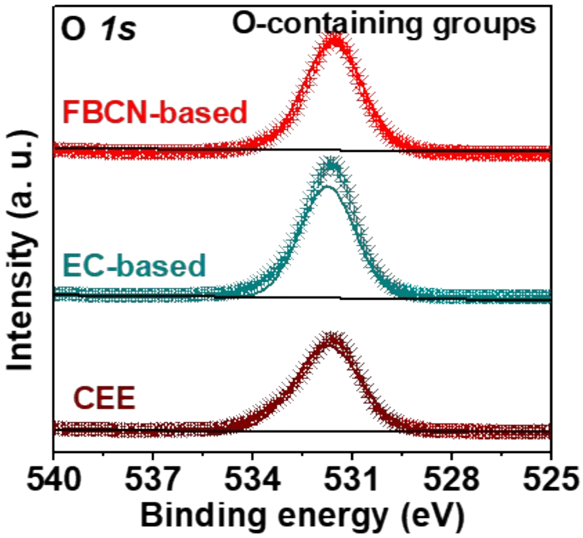

Figure S38. O signals for graphite cycled in various electrolyte.

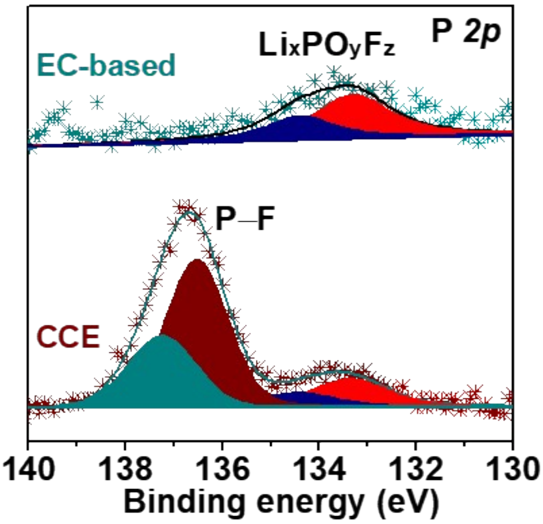

Figure S39. P signals for graphite cycled in various electrolytes.

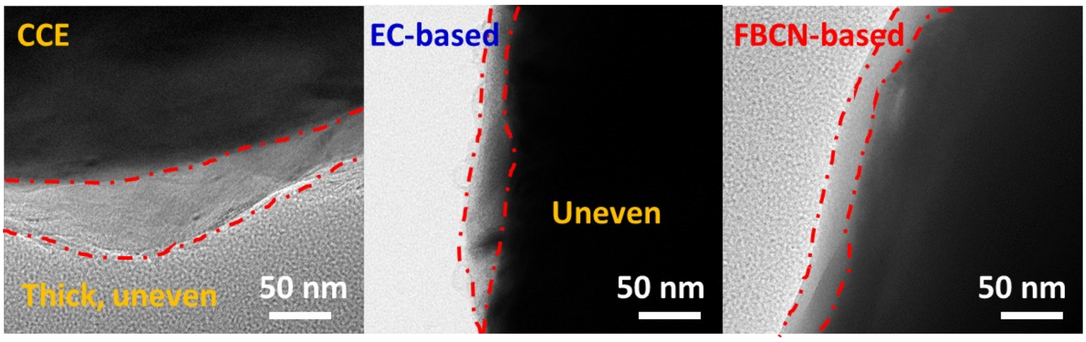

Figure S40. TEM images for graphite cycled in CCE, EC-based and FBCN-based electroltyes. The severe decomposition of carbonates in CCE leads to thick and uneven coverage on graphite. The SEI formed in EC-based electrlyte is still uneven despite modifications from additives. In contrast, a thin and uniform passivation is constructed in FBCN-based electrolyte.

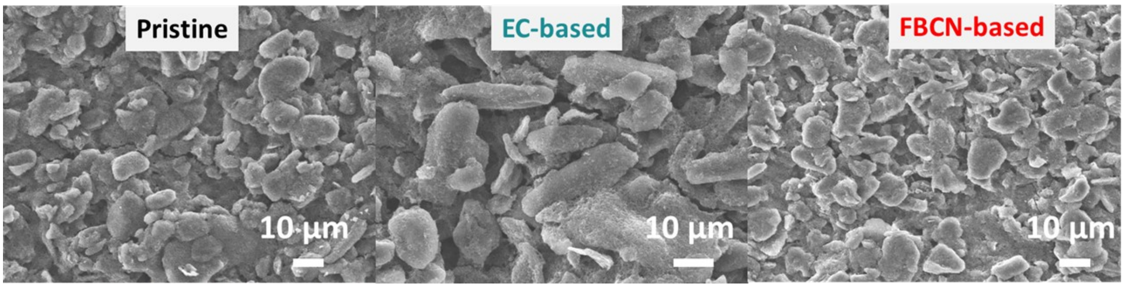

Figure S41. SEM images for graphite cycled in different electrolytes.

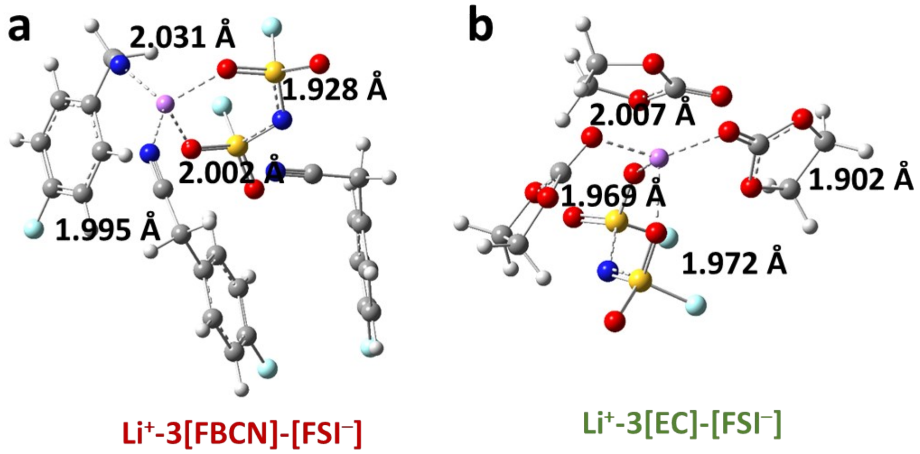

Figure S42. Optimized geometries for (a) Li^+-3[FBCN]-[FSI^-] and (b) Li^+-3[EC]-[FSI^-]. The enlarged distance for coordinated species in Li^+-3[FBCN]-[FSI^-] indicates a loose Li^+ solvation shell. Note that above geometries don't represent the practical solvates, but provide a comparison about the Li^+-solvents' binding strength. The results help with understanding the stability of FBCN-involved and EC-involved solvates from a theoretical side.

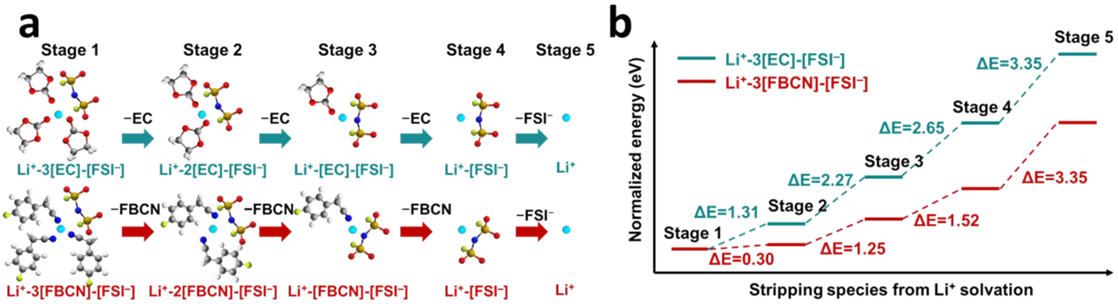

Figure S43. (a) Complete profiles and (b) corresponding energies for removing species in both EC-involved and FBCN-involved solvates. Note that the profile cannot reflect the true desolvation process and the values differ based on varied calculation model, but the always lower value for FBCN-involved solvates indeed supports its dynamic superiority over EC-involved solvates. Other interruptions including electric double layer, body effect and local electric field are discarded for simplicity in this calculation. The results indicate a higher energy-consuming step for removing EC from Li^+ solvates, which indicates the strong Li^+-EC binding from a theoretical side. The detailed calculations are listed in Table S2 and S3.

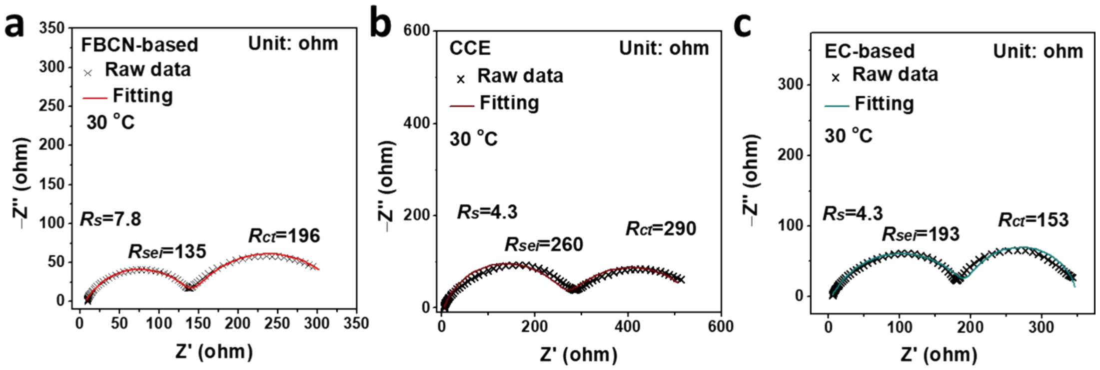

Figure S44. The fitting curves for graphite//graphite cells in (a) FBCN-based electrolyte, (b) CCE and (c) EC-based electrolyte.

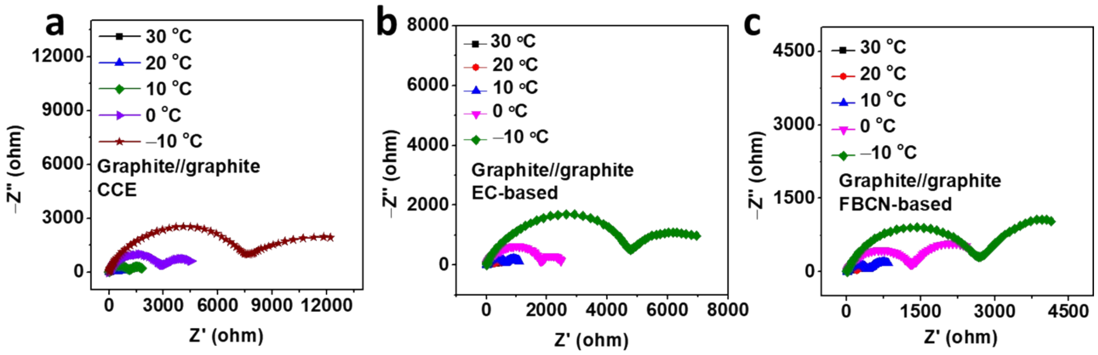

Figure S45. EIS results for graphite//graphite cells cycled in (a) CCE, (b) EC-based and (c) FBCN-based electrolytes.

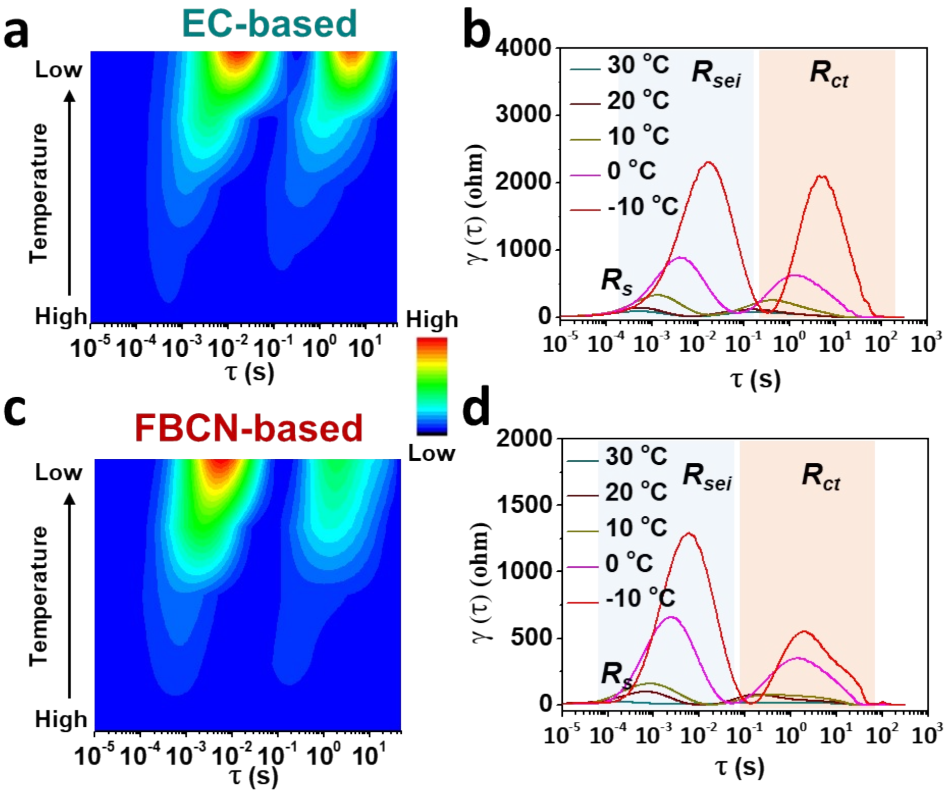

Figure S46. (a, c) The counter maps and (b, d) analyses of distribution of relaxation time (DRT) for symmetric cells in different temperatures. First, the R_s (at the highest frequency region) is negligible and tends to merge with R_{sei} at cold condition. Second, both R_{sei} and R_{ct} exhibit an Arrhenius relationship towards temperature variation. Third, the polarization of the impedance curve is increasing significantly and shifts to a lower frequency with decreasing temperature. Fourth, the R_{ct} is lower than R_{sei} for FBCN-based electrolyte, indicating the easy desolvation aroused from weak Li^+-FBCN binding. In contrast, the EC-based electrolyte still suffers from both high desolvation and sluggish Li^+ across SEI.

Table S1. Physical properties of common carbonates and FBCN. (EC: ethylene carbonate, PC: propylene carbonate, DMC dimethyl carbonate)[1, 2]

Solvent	FBCN	EC	PC	DMC
Molecular formula	C_8H_6FN	$C_3H_4O_3$	$C_4H_6O_3$	$C_3H_6O_3$
Molecular weight	135	88	102	90
Melting point (^oC)	None	36.4	-48.8	4.6
Boiling point (^oC)	238 (760 Torr)	248	242	91
Flash point (^oC)	108	160	132	18
Density (g cm^{-3})	1.1	1.3	1.2	1.1

Table S2. The calculations and energies for various species on graphite surface.

Species	Energy (eV)	Species	Energy (eV)	Calc.	$E_{ad.}$ (eV)
FBCN	−2255.79	1: Gra.+FBCN	−17430.99	$\Delta E=E_1-E_{Gra}-E_{FBCN}$	−0.67
EC	−1818.42	2: Gra.+EC	−16993.47	$\Delta E=E_2-E_{Gra}-E_{EC}$	−0.51
FEC	−2456.32	3: Gra.+FEC	−17631.23	$\Delta E=E_3-E_{Gra}-E_{FEC}$	−0.38
DMC	−1850.91	4: Gra.+DMC	−17025.93	$\Delta E=E_4-E_{Gra}-E_{DMC}$	−0.49
Gra.	−15174.53				

Table S3. The energies for various species in FBCN-dominated solvates.

Num.	Species	Energy (eV)	Process	Calc.	ΔE (eV)
1	Li^+-3[FBCN]-[FSI^-]	−74839.12	1-2	$\Delta E=E_2+E_7-E_1$	0.30
2	Li^+-2[FBCN]-[FSI^-]	−62232.21	2-3	$\Delta E=E_3+E_7-E_2$	1.25
3	Li^+-[FBCN]-[FSI^-]	−49624.35	3-4	$\Delta E=E_4+E_7-E_3$	1.52
4	Li^+-[FSI^-]	−37016.22	4-5	$\Delta E=E_5+E_6-E_4$	3.35
5	Li^+	−198.80			
6	FSI^-	−36814.07			
7	FBCN	−12606.61			

Table S4. The energies for various species in EC-dominated solvates.

Num.	Species	Energy (eV)	Process	Calc.	ΔE (eV)
1	Li^+-3[EC]-[FSI^-]	−64999.87	1-2	$\Delta E=E_2+E_7-E_1$	1.31
2	Li^+-2[EC]-[FSI^-]	−55672.75	2-3	$\Delta E=E_3+E_7-E_2$	2.27
3	Li^+-[EC]-[FSI^-]	−46344.68	3-4	$\Delta E=E_4+E_7-E_3$	2.65
4	Li^+-[FSI^-]	−37016.22	4-5	$\Delta E=E_5+E_6-E_4$	3.35
5	Li^+	−198.80			
6	FSI^-	−36814.07			
7	EC	−9325.81			

References：

1. k. Xu, Chem. Rev., 2004, 104, 4303−4417.

2. J. Velcicky, A. Soicke, R. Steiner and H. G. Schmalz, 2011, 133, 6948-6951.